IEEE Access
Multidisciplinary ⋮ Rapid Review ⋮ Open Access Journal

Received 25 September 2023, accepted 7 October 2023, date of publication 11 October 2023, date of current version 17 October 2023.

Digital Object Identifier 10.1109/ACCESS.2023.3323694

RESEARCH ARTICLE

Automatic Recognition of Illegal Substations by Employing Logit-Boost Algorithm and LSTM With the Help of Different Landsat-8 OLI Image Spectral Band Parameters: A Case Study in Sason, Turkey

EMRULLAH ACAR[1], ENES BAKIŞ[2], AND MUSA YILMAZ[1,3], (Senior Member, IEEE)
[1]Department of Electrical and Electronics Engineering, Faculty of Engineering and Architecture, Batman University, 72000 Batman, Turkey
[2]Department of Electrical and Electronics Engineering, Faculty of Engineering, Piri Reis University, 34940 Istanbul, Turkey
[3]Center for Environmental Research and Technology, Bourns College of Engineering, University of California at Riverside, Riverside, CA 92521, USA

Corresponding author: Musa Yilmaz (musay@ucr.edu)

ABSTRACT Automatic recognition of illegal substations is of great importance, since most of the leakage electricity in Turkey is due to the use of these substations in agricultural fields. One of the most effective ways to detect illegal substations is to employ remote sensing images and machine learning techniques together. Because, thanks to remote sensing images, it is possible to analyze illegal substations on huge agricultural lands in a short time. In this study, illegal substations on the agricultural fields in the southeast Anatolian region, which is one of the regions where leakage electricity are most common, have been detected with the aid of Landsat-8 OLI images and machine learning algorithm. The proposed study has been carried out in several stages, respectively. In the first stage, the locations of 42 substations and 21 non-substation objects on the pilot area have been recorded with the help of GPS and these coordinates have been later transferred to the Landsat-8 OLI image dated on 14 June 2019. In the second stage, an image analysis has been performed by calculating the spectral band parameters from the Landsat-8 OLI images. In the next stage, relationships among illegal substations and non-substation objects have been set by utilizing the statistical metrics of obtained spectral band parameters. In the last stage, by utilizing LSTM (Long Short-Term Memory) method, which is a recurrent neural network model that has gained popularity in both remote sensing and various scientific disciplines in recent years and the Logit-Boost method, which is one of the popular boosting machine learning algorithms, automatic recognition of substations has been performed with an average accuracy of 88.89% for Logit-Boost method and 84.21% for LSTM method. It is notable from this study that the Logit-Boost Algorithm yields more proficient results than the LSTM model.

INDEX TERMS Substation recognition, image analysis, landsat-8, Logit-Boost algorithm, LSTM.

I. INTRODUCTION

Object identification with the help of remote sensing images is a fundamental challenge in the field of satellite imaging and their analysis. However, object detection has gained great attention in recent years and plays an important role in a wide range of applications [1]. Identification of objects on large areas with traditional methods and modern measurement techniques requires a lot of expense, time and labor intensity [2]. These difficulties in determining objects over the lands can be overcome by employing remote sensing technologies.

In this context, with the recent development of medium or high spatial resolution satellite images and the easy production of spatial and spectral information, less costly results

The associate editor coordinating the review of this manuscript and approving it for publication was Jeon Gwanggil.

can be obtained in a shorter time on large areas without requiring much workload [3]. In the literature, many studies have been carried out using remote sensing data. These studies are generally discussed under two main headings as active (Sentinel-1, Radarsat-1, Radarsat-2, etc…) and passive (Sentinel-2, Landsat-8, MODIS, etc…) systems. Some of the most studies using passive remote sensing systems with image processing or machine learning techniques are summarized as follows.

Acar and Altun proposed a system in order to classify agricultural crops (Lentil and Wheat) by utilizing Support Vector Machine (SVM) technique and Landsat-8 Normalized Difference Vegetation Index parameters. As a result, a high overall accuracy was observed for crop classification [4]. Balogun et al. employed multispectral Landsat 8-OLI image and machine learning models (Support Vector Machine and Random Forest) to determine the effects of oil spills over coastal wetland and vegetation. Moreover, they monitored the recovery pattern of polluted wetland and vegetation in a coastal city, Malaysia [5]. Sekandari et al. recommended an approach in order to identify Zn-Pb mineralization in the Kashmar–Kerman Tectonic Zone and the Central Iranian Terrane by utilizing different satellite images (Sentinel-2, ASTER, Landsat-8 and WorldView-3) and Principal Component Analysis (PCA) based fuzzy logic modeling. The results indicated that spectral data obtained from multi-sensor remote sensing images can be widely employed to generate remote sensing-based probability maps for the research of Pb-Zn mineralization in many metallogenic provinces around the worldwide [6]. Vanhellemont investigated the land and water surface temperature by employing the performances of the Thermal Infrared Sensor (TIRS) single-band reuptakes in Landsat-8. As a result, a very temporal terrain method was demonstrated based on images obtained from the Landsat-8 and it was determined that it would be possible to provide precise absolute surface temperature [7]. Beiranvand Pour et al. proposed a system for mineral prospecting and mapping of hydrothermal alteration in the Inglefield Land, Northwest Greenland with the aid of various satellite images (ASTER, Landsat-8 and WorldView-3) and image processing techniques (Directed Principal Components Analysis, Linear Spectral Unmixing, Adaptive Coherence Estimator). The result showed that the differentiation of lithological units and zones include high concentration of clay minerals, iron oxides/hydroxide in the Inglefield Mobile Belt were accomplished by utilizing Landsat-8 image at the regional scale [8]. Golhani et al. suggested a system in order to detect orange spotting disease in oil palm by employing Red Edge and four spectral indices (simple ratio, red edge normalized difference vegetation index, two-band enhanced vegetation index 2 and chlorophyll index red edge). Moreover, they implemented multilayer perceptron neural network to build a nonlinear correlation among selected each spectral index and spectral bands. As a result, a highest correlation was observed between two-band enhanced vegetation index 2 and spectral bands [9]. Fan et al. utilized Landsat-8 Operational Land Imager (OLI) Surface Reflection (SR), Visible Infrared Imaging Radiometer Suite and MODIS methods to detect earthquake damage areas. The data in the methods were applied to the Nepal earthquake with a magnitude of 7.8 in 2015 and they determined that there was not much difference between the obtained results and the estimated damaged pixels [10]. He et al. employed Landsat-8 satellite data to classify the effect of temperature on improving or reducing land surface temperature in Shenyang, China, at seven temperature levels and evaluated the relationship between land covers and their use [11]. Fang et al. compared deep learning methods and traditional machine learning methods using convolutional neural network (CNN)-based Landsat-8 satellite images to identify man-made global reservoirs [12]. Kuhn et al. compared Landsat-8 and Sentinel-2 reflectance products on rivers to indicate the relationship between satellite recovery on rivers, absorption and scattering properties of river water with remote sensing reflection [13]. Lamqadem et al. proposed an approach for mapping the amount of desertification in middle Draa Valley, Morocco by utilizing Spectral Index Techniques and Sentinel-2 image. The result showed that the proposed system is effective for mapping desertification with high accuracy [14]. Sameen et al. recommended a system for classifying aerial photographs into seven classes (grassland, road, building, waterbody, barren land, dense vegetation and shadow) with the help of convolutional neural network. Their proposed work demonstrated that CNN-based approaches can be utilized efficiently for land cover classification using aerial photographs [15]. Man et al. examined seven land classes utilizing high spatial resolution Landsat-8 satellite images by creating time series composite images from five supervised classifiers and using merging techniques to obtain maps of land cover types. As a result, they found that the resulting composite images were 20% more successful than the first images [16]. Arslan applied different image processing techniques (such as minimum noise fraction, convolution filters) to Landsat-8 bands in the detection of oil spill areas formed when a ship ran aground in Ildır Bay, İzmir. Finally, they obtained successful results by analyzing oil spill areas with the location of the ship [17]. Wang et al. analyzed radiation anomalies in a Gaussian Mixture Model with a new ship object detection method in the ocean using Landsat-8 satellite imagery as the long wavelength infrared band. As a result, they found the ship detection accuracy of this method with higher recall, unlike other classical methods [18]. Barnes and Hu determined an underwater coral reef area longer than 15 km using Landsat-8 satellite data for island construction in the South China Sea between 2013 and 2015, and evaluated water turbidity using MODIS data [19]. Avdan and Jovanovska developed a new algorithm using Landsat-8 thermal infrared sensor Band 10 data on land surface temperature. Then, to determine the accuracy of this algorithm, they compared the temperatures near the land surface and the air and found that the deviation was low [20]. Wieland

and Pittore evaluated the effect of Landsat-8 satellite data on SVM performance to define settlement type classification and urban building types based on the images of 43 settlements in Central Asia. As a result, they stated that these data used were sufficient and satisfactory for the classification tasks [21]. Jagalingam et al. determined bathymetry mapping by utilizing the blue and green bands of the Landsat-8 satellite due to open and free access to detect the bathymetry of the coasts in India and a good correlation was obtained between the results obtained and the hydrographic sounding values [22]. Acar tried to detect the EDTs on agricultural lands in Diyarbakir by using the Sentinel-1 SAR satellite data by machine learning method. He used ELM (Extreme Machine Learning) in his study and achieved an accuracy rate of 85.47% [23].

In this study, an image analysis has been performed by calculating the spectral band parameters from the Landsat-8 OLI images and relationships among substations and non-substation objects have been set by utilizing the statistical metrics of obtained spectral band parameters. Moreover, one of the most popular boosting algorithms and LSTM method have been employed in order to recognize illegal substations.

This study has two main contributions. One of these contributions is that a comparative image analysis has been performed by calculating the spectral band parameters from the substations and non-substation objects thanks to the statistical metrics of obtained Landsat-8 OLI spectral band parameters. Another contribution is that illegal substations in agricultural fields, which cause huge energy losses in Turkey, have been recognized automatically with the help of feature vectors to be created from the Landsat-8 OLI spectral band parameters, Logit-Boost Algorithm and LSTM.

The rest of the manuscript is organized as follows: the image pre-processing steps is detailed in Section II. Afterward, the experimental results on determining of the spectral band parameters are presented in Section III. A comprehensive discussion is given in Section IV. Finally, the proposed approach is summed up in Section V.

II. MATERIALS AND METHODS

A. THE EXPERIMENTAL AREA

In this study, the area where the substations and non-substation objects are located within the boundaries of Sason district of Batman province was chosen as the pilot region. The location of the experimental area and different samples (the dots in the satellite image) in this area are shown in Fig.1.

B. LANDSAT-8 OLI DATA ACQUISITION

Landsat-8 was launched on February 4, 2013 from Vandenberg Air Force Base, California. In this study, one LANDSAT/LC08/C01/T1 (Landsat 8, Collection 1, Tier 1) OLI satellite image courtesy of the U.S. Geological Survey belonging to 14 June 2019 was obtained by employing google earth engine code editor platform (https:// code. earthengine. google. com). Google Earth Engine is a cloud-based platform that performs it effortless to access high-performance computing facilities for processing numerous wide geospatial datasets [24]. The color image obtained by combining three different bands (Band 2+ Band 3+ Band 4) of the Landsat-8 OLI image covering the study area is shown in Fig. 2.

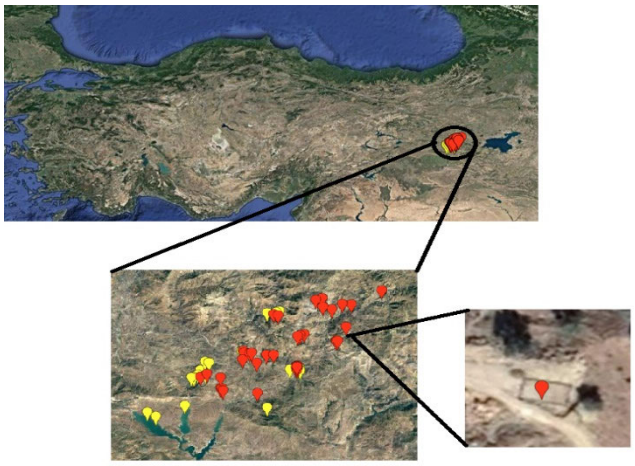

FIGURE 1. The position of the experimental area with the different substations (red points) and non-substation (yellow points) samples.

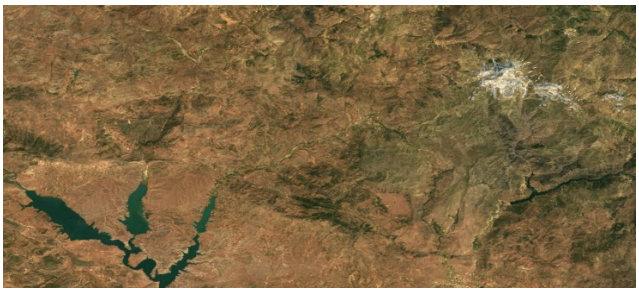

FIGURE 2. The color Landsat-8 OLI image obtained covering the study area.

C. GROUND DATA COLLECTION

At this stage, the geographical coordinates of 42 different substations and 21 non-substations were recorded with the help of GPS device and then these data were imported to LANDSAT/LC08/C01/T1 OLI image with the aid of Google earth engine code editor as shown in Fig. 3.

D. FEATURE EXTRACTION FROM LANDSAT-8 OLI IMAGE

The Landsat-8 OLI data is the atmospherically corrected surface reflectance from the Landsat 8 OLI/TIRS sensors. This image includes 9 spectral bands which are 2 thermal infrared (TIR) bands, 2 short-wave infrared (SWIR) bands and 5 visible and near-infrared (VNIR) bands. The pixel resolution for Landsat-8 OLI Image is 30 m. The detailed information about the Landsat-8 OLI spectral band parameters are given in Table 1 [25].

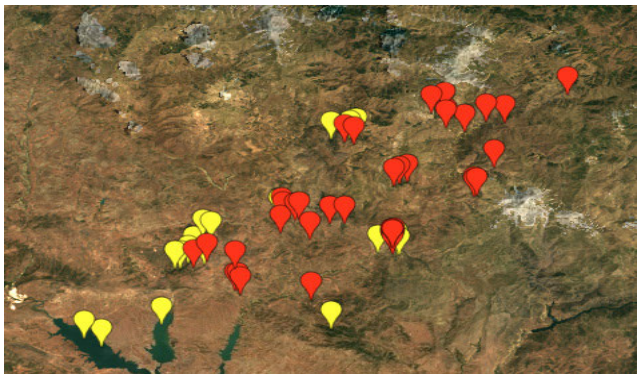

FIGURE 3. Importing of the geographical coordinates of 42 different substations (red points) and 21 non-substations (yellow points) into the color Landsat-8 OLI image.

TABLE 1. Landsat-8 OLI spectral band parameters.

Spectral Bands	Wavelengths (μm)	Description
B1	435-451	Ultra Blue
B2	452-512	Blue
B3	533-590	Green
B4	636-673	Red
B5	851-879	Near Infrared
B6	1566-1651	Shortwave Infrared 1
B7	2107-2294	Shortwave Infrared 2

At this stage, the pixel values of the substation and non-substation samples corresponding to seven different spectral bands (B1-B7) of the Landsat-8 OLI data were calculated. However, (B10- B11) spectral bands were not evaluated because they are obtained using the Landsat 8 TIRS sensor. Consequently, feature vectors of seven-unit lengths were created for each sample point and this procedure is given in detail in the section III.

E. LOGIT-BOOST ALGORITHM

Logit-Boost is one of the popular boosting algorithms in machine learning and it is formulated by Jerome Friedman, Trevor Hastie, and Robert Tibshirani. This algorithm can be derived from the Ada-Boost algorithm because both are similar in the point of performing an additive logistic regression. The difference between them is that. Ada-Boost diminishes exponential loss, while Logit-Boost reduces logistic loss. Moreover, the Logit-Boost algorithm is more convenient in order to handle the noisy data on the widely employed Ada-boost algorithm [26]. The Logit-Boost algorithm includes the following stages, respectively.

- Assume that input dataset contains N samples with input number of iterations K

$$N = \{(x_1, y_1), (x_2, y_2), \ldots, (x_i, y_i)\} \quad i = 1, 2, \ldots, N \tag{1}$$

Here, x_i and y_i represent input feature vectors and target, respectively.

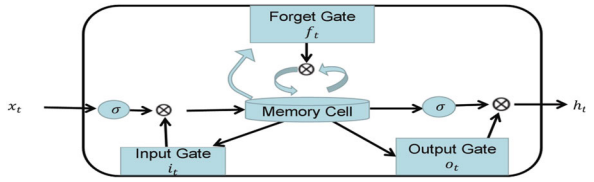

FIGURE 4. The schematic of long short-term memory.

- Start the weights $w_i = \frac{1}{N}$, probabilities estimates $P(x_i) = \frac{1}{2}$ and initialize committee function $F(x) = 0$.
- Compute weights (w_i) and working response (z_i) by repeating for $k = 1, 2, \ldots, K$

$$w_i = P(x_i)(1 - P(x_i)) \tag{2}$$

$$z_i = \frac{y_i - P(x_i)}{P(x_i)(1 - P(x_i))} \tag{3}$$

- Fit $Fk(x)$ with a weighted least squares regression from z_i to x_i by employing w_i and then update the functions as indicated in Equation-4 and Equation-5.

$$F(x) \leftarrow F(x) + \frac{1}{2} Fk(x) \tag{4}$$

$$p(x) \leftarrow \frac{e^{F(x)}}{e^{-F(x)} + e^{F(x)}} \tag{5}$$

- Finally, the output of classifier becomes:

$$sign[F(x)] = sign\left[\sum_{k=1}^{K} Fk(x)\right] \tag{6}$$

Here, $sign[F(x)]$ has two output classes as shown in Equation-7.

$$sign[F(x)] = \begin{cases} -1 & if\ F(x) \geq 0 \\ +1 & if\ F(x) < 0 \end{cases} \tag{7}$$

F. LSTM METHOD

The LSTM neural network is a variant of the Recurrent Neural Networks (RNN) [27]. Compared to RNN, LSTM can handle both long-term dependence problems and reduce the possibility of gradient disappearance [28].

The core concept of LSTM is the cell state and the gate structure, cell states can convey information and overcome the effects of short-term memory. The LSTM has three types of gate structures: input, forgetting, and output gates, each of which has its unique role. The structure of LSTM method is shown in Fig. 4 [29].

- The equations for the gates in the LSTM method are as follows;

$$i_t = \sigma(w_i + [h_{t-1}, x_t] + b_i) \tag{8}$$

$$f_t = \sigma(w_f + [h_{t-1}, x_t] + b_f) \tag{9}$$

$$o_t = \sigma(w_o + [h_{t-1}, x_t] + b_o) \tag{10}$$

i_t = Represents the input gate.
f_t = Represents the forget gate.
o_t = Represents the output gate.

σ = Represents the sigmoid function.
w_x = Weight values for the corresponding gate(x) neuron.
h_{t-1} = Represents the output of the previous LSTM block.
x_t = Input value to the current time loop.
b_t = Threshold values for the corresponding gate(x) neuron.

- The equations for cell state, candidate cell state and final output in the LSTM model are as follows;

$$\tilde{c}_t = tanh(w_c * [h_{t-1}, x_t] + b_c) \quad (11)$$
$$c_t = (f_t * c_{t-1}) + (i_t * \tilde{c}_t) \quad (12)$$
$$h_t = o_t * \tanh(c^t) \quad (13)$$

c_t = Represents the cell state (memory) in the time loop.
$\tilde{c}_t$ = Represents the candidate cell state (memory) in the time loop.
$*$ = Multiplication process

G. STATISTICAL METRICS

In this phase, two statistical metrics, mean (μ) and standard deviation (σ), were utilized to observe the relationship between different spectral band parameters of substations and non-substation samples. Equations of these metrics are given below, respectively.

$$\mu = 1/n \sum_{i=1}^{n} Xi \quad (14)$$
$$\sigma = \sqrt{\frac{\sum (X-\mu)^2}{n-1}} \quad (15)$$

Here; Xi is the value in data distribution and n is the total number of observations. Additionally, five performance metrics were computed for proposed system by employing the following equations. Furthermore, confusion matrix, ROC curve and Accuracy Graphs were used for demonstrating the success of LSTM method.

$$\text{Sensitivity} = \frac{TP}{TP+FN} \quad (16)$$
$$\text{Specificity} = \frac{TN}{TN+FP} \quad (17)$$
$$\text{Precision} = \frac{TP}{TP+FP} \quad (18)$$
$$\text{F1-Score} = \frac{2TP}{2TP+FP+FN} \quad (19)$$
$$\text{Accuracy} = \frac{TP+TN}{TP+TN+FP+FN} \quad (20)$$

Here, TP, TN FP, and FN represent true positive, true negative, false positive, and false negative numbers, respectively.

III. RESULTS

In this section, spectral band images of the preprocessed Landsat-8 OLI data are presented as below. Feature vectors (spectral band parameters) were then calculated from pixels corresponding to substations and non-substation samples in these spectral band images and relationships among substations were set by employing the statistical metrics of obtained spectral band parameters. Moreover, one of the most popular boosting algorithms and LSTM was utilized for recognizing substations with the aid of obtained datasets.

TABLE 2. Obtaining B1 (ultra blue) spectral band parameters for substations.

Substation Number	B1 Parameter	Substation Number	B1 Parameter
S1	544	S22	533
S2	521	S23	704
S3	544	S24	378
S4	511	S25	613
S5	640	S26	471
S6	419	S27	613
S7	511	S28	525
S8	511	S29	655
S9	795	S30	471
S10	576	S31	585
S11	400	S32	570
S12	640	S33	471
S13	643	S34	585
S14	795	S35	568
S15	795	S36	568
S16	618	S37	410
S17	652	S38	404
S18	666	S39	324
S19	586	S40	481
S20	394	S41	384
S21	349	S42	388
Mean (μ)			543.12
Standard Deviation (σ)			119.88

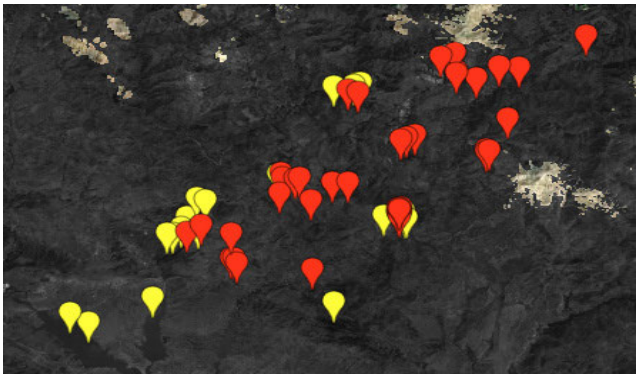

FIGURE 5. The image corresponding to the B1 (ultra blue) band of Landsat-8 OLI data.

A. OBTAINING B1 SPECTRAL BAND PARAMETERS

In this part, the image corresponding to the B1 (Ultra Blue) band of Landsat-8 OLI data is shown in Fig. 5. Furthermore, the spectral band parameter values of the pixels corresponding to 42 substations (red points) and 21 non-substation samples (yellow points) in this band with statistical metrics (μ and σ) are given in Table 2 and Table 3, respectively.

TABLE 3. Obtaining B1 (ultra blue) spectral band parameters for non-substations.

Non-Substation Number	B1 Parameter
NS1	462
NS2	462
NS3	462
NS4	462
NS5	661
NS6	433
NS7	433
NS8	433
NS9	433
NS10	433
NS11	392
NS12	392
NS13	392
NS14	392
NS15	455
NS16	455
NS17	493
NS18	493
NS19	726
NS20	472
NS21	630
Mean (μ)	**474.57**
Standard Deviation (σ)	**89.47**

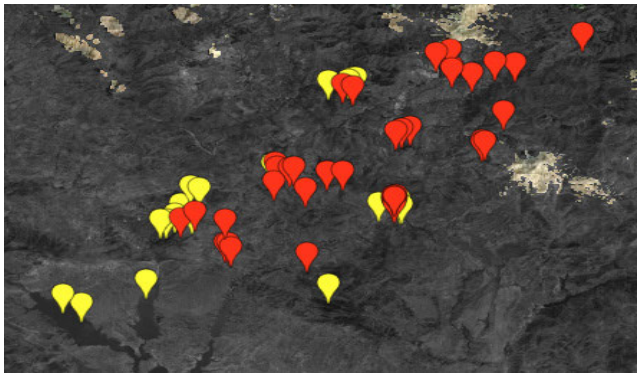

FIGURE 6. The image corresponding to the B2 (blue) band of Landsat-8 OLI data.

As seen in the Table 2, the mean surface reflection values of 42 different substations in the B1 spectral band was calculated as 543.12 and the standard deviation as 119.88.

As seen in Table 3, the mean surface reflection values of 21 different non-substation objects in the B1 spectral band was computed as 474.57 and the standard deviation as 89.47.

B. OBTAINING B2 SPECTRAL BAND PARAMETERS

In this step, the image corresponding to the B2 (Blue) band of Landsat-8 OLI data is indicated in Fig. 6 and the spectral band parameter values of the different substations and non-substation samples are given in Table 4 and Table 5, respectively.

In the Table 4, the mean surface reflection values of different substations in the B2 spectral band was computed as 729.09 and the standard deviation as 166.45.

TABLE 4. Obtaining B2 (ultra blue) spectral band parameters for substations.

Substation Number	B2 Parameter	Substation Number	B2 Parameter
S1	774	S22	709
S2	746	S23	931
S3	774	S24	575
S4	698	S25	812
S5	908	S26	653
S6	598	S27	812
S7	698	S28	694
S8	698	S29	822
S9	1068	S30	580
S10	845	S31	686
S11	574	S32	756
S12	908	S33	636
S13	897	S34	821
S14	1068	S35	703
S15	1068	S36	703
S16	861	S37	530
S17	879	S38	492
S18	889	S39	429
S19	736	S40	630
S20	534	S41	487
S21	409	S42	531
Mean (μ)			**729.09**
Standard Deviation (σ)			**166.45**

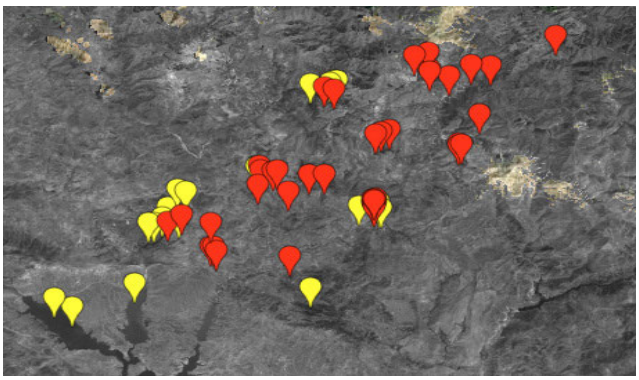

FIGURE 7. The image corresponding to the B3 (green) band of Landsat-8 OLI data.

As seen in the Table 5, the mean surface reflection values of 21 different non-substation objects in the B2 spectral band was calculated as 624.09 and the standard deviation as 117.12.

C. OBTAINING B3 SPECTRAL BAND PARAMETERS

In this stage, the image corresponding to the B3 (Green) band of Landsat-8 OLI data is illustrated in Fig. 7 and the spectral band parameter values of the different substations and non-substation samples are presented in Table 6 and Table 7, respectively.

As seen in the Table 6, the mean surface reflection values of different substations in the B3 spectral band was calculated as 1181.23 and the standard deviation as 235.28.

TABLE 5. Obtaining B2 (ultra blue) spectral band parameters for non-substations.

Non-Substation Number	B2 Parameter
NS1	627
NS2	627
NS3	627
NS4	627
NS5	877
NS6	586
NS7	586
NS8	586
NS9	586
NS10	586
NS11	509
NS12	509
NS13	509
NS14	509
NS15	618
NS16	618
NS17	545
NS18	545
NS19	902
NS20	660
NS21	867
Mean (μ)	**624.09**
Standard Deviation (σ)	**117.12**

TABLE 6. Obtaining B3 (ultra blue) spectral band parameters for non-substations.

Substation Number	B3 Parameter	Substation Number	B3 Parameter
S1	1298	S22	1131
S2	1222	S23	1420
S3	1298	S24	1047
S4	1190	S25	1231
S5	1456	S26	1058
S6	1056	S27	1231
S7	1190	S28	1076
S8	1190	S29	1268
S9	1652	S30	959
S10	1405	S31	1023
S11	1032	S32	1245
S12	1456	S33	1023
S13	1450	S34	1326
S14	1652	S35	1101
S15	1652	S36	1101
S16	1329	S37	894
S17	1359	S38	825
S18	1378	S39	696
S19	1232	S40	998
S20	952	S41	849
S21	711	S42	950
Mean (μ)			**1181.23**
Standard Deviation (σ)			**235.28**

As illustrated in the Table 7, the mean surface reflection values of 21 different non-substation objects in the B3 band was computed as 958.33 and the standard deviation as 188.60

D. OBTAINING B4 SPECTRAL BAND PARAMETERS

In this phase, the image corresponding to the B4 (Red) band of Landsat-8 OLI data is indicated in Fig. 8 and the spectral band parameter values of the different substations and non-substation objects are tabulated in Table 8 and Table 9, respectively.

TABLE 7. Obtaining B3 (ultra blue) spectral band parameters for non-substations objects.

Non-Substation Number	B3 Parameter
NS1	943
NS2	943
NS3	943
NS4	943
NS5	1337
NS6	965
NS7	965
NS8	965
NS9	965
NS10	965
NS11	793
NS12	793
NS13	793
NS14	793
NS15	982
NS16	982
NS17	666
NS18	666
NS19	1300
NS20	1069
NS21	1354
Mean (μ)	**958.33**
Standard Deviation (σ)	**188.60**

TABLE 8. Obtaining B4 (ultra blue) spectral band parameters for substations.

Substation Number	B4 Parameter	Substation Number	B4 Parameter
S1	1564	S22	1380
S2	1453	S23	1889
S3	1564	S24	1162
S4	1454	S25	1702
S5	1817	S26	1369
S6	1198	S27	1702
S7	1454	S28	1363
S8	1454	S29	1593
S9	2078	S30	1043
S10	1682	S31	1262
S11	1106	S32	1475
S12	1817	S33	1272
S13	1832	S34	1669
S14	2078	S35	1347
S15	2078	S36	1347
S16	1798	S37	1044
S17	1740	S38	954
S18	1844	S39	791
S19	1427	S40	1111
S20	977	S41	907
S21	601	S42	1046
Mean (μ)			**1439.14**
Standard Deviation (σ)			**360.33**

As shown in the Table 8, the mean surface reflection values of different substations in the B4 spectral band was computed as 1439.14 and the standard deviation as 360.33.

When the values in Table 9 are examined, the mean surface reflection values of 21 different non-substation objects in the

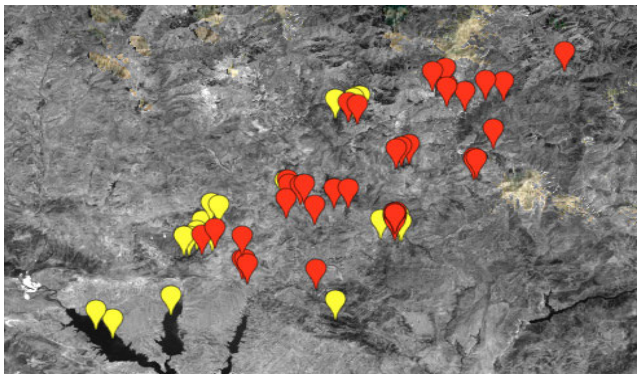

FIGURE 8. The image corresponding to the B4 (red) band of Landsat-8 OLI data.

TABLE 9. Obtaining B4 (ultra blue) spectral band parameters for non-substations objects.

Non-Substation Number	B4 Parameter
NS1	1248
NS2	1248
NS3	1248
NS4	1248
NS5	1853
NS6	1143
NS7	1143
NS8	1143
NS9	1143
NS10	1143
NS11	912
NS12	912
NS13	912
NS14	912
NS15	1189
NS16	1189
NS17	266
NS18	266
NS19	1717
NS20	1409
NS21	1727
Mean (μ)	**1141.47**
Standard Deviation (σ)	**390.21**

B4 spectral band was calculated as 1141.47 and the standard deviation as 390.21.

E. OBTAINING B5 SPECTRAL BAND PARAMETERS

In this step, the image corresponding to the B5 (Near Infrared) band of Landsat-8 OLI data is shown in Fig. 9 and the spectral band parameter values of the different substations and non-substation objects are represented in Table 10 and Table 11, respectively.

As illustrated in the Table 10, the mean surface reflection values of different substations in the B5 spectral band was calculated as 3302.11 and the standard deviation as 371.73.

When the values in Table 11 are evaluated, the mean surface reflection values of 21 different non-substation objects in the B5 spectral band was calculated as 2807.39 and the standard deviation as 928.21.

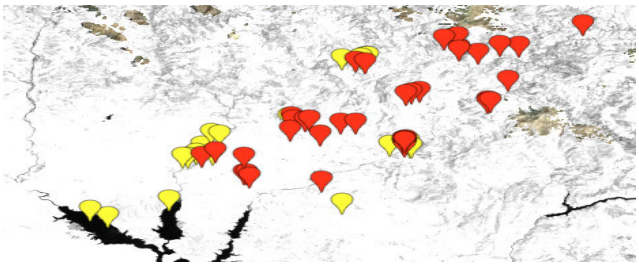

FIGURE 9. The image corresponding to the B5 (near infrared) band of Landsat-8 OLI data.

TABLE 10. Obtaining B5 (ultra blue) spectral band parameters for substations.

Substation Number	B5 Parameter	Substation Number	B5 Parameter
S1	3780	S22	3497
S2	3413	S23	3231
S3	3780	S24	3556
S4	3496	S25	3239
S5	2943	S26	3794
S6	3474	S27	3239
S7	3496	S28	3213
S8	3496	S29	3042
S9	3183	S30	3017
S10	3128	S31	2151
S11	3654	S32	2874
S12	2943	S33	3449
S13	3292	S34	3627
S14	3183	S35	2847
S15	3183	S36	2847
S16	3245	S37	3322
S17	3758	S38	3087
S18	3904	S39	2673
S19	3284	S40	2767
S20	3619	S41	3890
S21	3834	S42	3239
Mean (μ)			**3302.11**
Standard Deviation (σ)			**371.73**

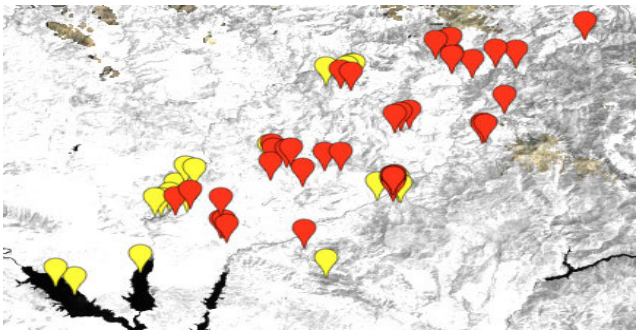

FIGURE 10. The image corresponding to the B6 (shortwave infrared 1) band of Landsat-8 OLI data.

F. OBTAINING B6 SPECTRAL BAND PARAMETERS

In this part, the image corresponding to the B6 (Shortwave Infrared 1) band of Landsat-8 OLI data is indicated in Fig. 10 and the spectral band parameter values of the different substations and non-substation objects are given in Table 12 and Table 13, respectively.

TABLE 11. Obtaining B5 (ultra blue) spectral band parameters for non-substations.

Non-Substation Number	B5 Parameter
NS1	3265
NS2	3262
NS3	3265
NS4	3265
NS5	3745
NS6	2922
NS7	2922
NS8	2922
NS9	2922
NS10	2922
NS11	2838
NS12	2838
NS13	2838
NS14	2838
NS15	3392
NS16	3392
NS17	118
NS18	118
NS19	2869
NS20	3354
NS21	2948
Mean (μ)	**2807.39**
Standard Deviation (σ)	**928.84**

TABLE 12. Obtaining B6 (ultra blue) spectral band parameters for substations.

Substation Number	B6 Parameter	Substation Number	B6 Parameter
S1	3274	S22	2915
S2	2884	S23	3230
S3	3274	S24	2484
S4	2825	S25	3157
S5	2995	S26	3072
S6	2595	S27	3157
S7	2825	S28	2947
S8	2825	S29	3342
S9	3206	S30	2229
S10	2944	S31	2503
S11	2445	S32	3028
S12	2995	S33	2989
S13	3185	S34	3063
S14	3206	S35	2454
S15	3206	S36	2454
S16	3435	S37	2652
S17	3421	S38	2550
S18	3407	S39	1881
S19	3029	S40	2213
S20	2532	S41	2484
S21	2024	S42	2285
Mean (μ)			**2848.11**
Standard Deviation (σ)			**399.50**

As indicated in the Table 12, the mean surface reflection values of different substations in the B6 spectral band was computed as 2848.11 and the standard deviation as 399.50.

As illustrated in Table 13, the mean surface reflection values of 21 different non-substation objects in the B5 spectral band was calculated as 2417.23 and the standard deviation as 836.60.

TABLE 13. Obtaining B6 (ultra blue) spectral band parameters for non-substations objects.

Non-Substation Number	B6 Parameter
NS1	2685
NS2	2685
NS3	2685
NS4	2685
NS5	3522
NS6	2395
NS7	2395
NS8	2395
NS9	2395
NS10	2395
NS11	2481
NS12	2484
NS13	2481
NS14	2481
NS15	2744
NS16	2744
NS17	64
NS18	64
NS19	3331
NS20	2723
NS21	2928
Mean (μ)	**2417.23**
Standard Deviation (σ)	**836.60**

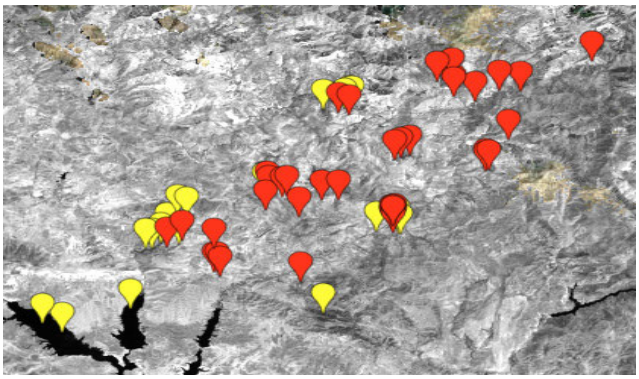

FIGURE 11. The image corresponding to the B7 (shortwave infrared 2) band of Landsat-8 OLI data.

G. OBTAINING B7 SPECTRAL BAND PARAMETERS

In this step, the image corresponding to the B7 (Shortwave Infrared 2) band of Landsat-8 OLI data is illustrated in Fig. 11 and the spectral band parameter values of the different substations and non-substation objects are tabulated in Table 14 and Table 15, respectively.

As presented in the Table 14, the mean surface reflection values of different substations in the B7 spectral band was calculated as 3171.47 and the standard deviation as 405.21.

As seen in the Table 15, the mean surface reflection values of 21 different non-substation objects in the B7 band was computed as 1542.80 and the standard deviation as 558.50.

H. DETERMINING RELATIONSHIPS AMONG SUBSTATIONS

At this stage, a dataset corresponding to the all substations were generated as presented in Table 15 and the correlations of these substations are given in Fig. 12.

TABLE 14. Obtaining B7 (ultra blue) spectral band parameters for substations.

Substation Number	B7 Parameter	Substation Number	B7 Parameter
S1	3780	S22	3497
S2	3413	S23	3231
S3	3780	S24	3556
S4	3496	S25	3239
S5	2943	S26	3794
S6	3474	S27	3239
S7	3496	S28	3213
S8	3496	S29	3042
S9	3183	S30	3017
S10	3128	S31	2151
S11	3654	S32	2874
S12	2943	S33	3449
S13	3292	S34	3627
S14	3183	S35	2847
S15	3183	S36	2847
S16	3245	S37	3322
S17	3758	S38	3087
S18	3904	S39	2673
S19	3284	S40	2767
S20	3619	S41	3890
S21	3834	S42	3239
Mean (μ)			**3171.47**
Standard Deviation (σ)			**405.21**

TABLE 15. Obtaining B7 (ultra blue) spectral band parameters for non-substations.

Non-Substation Number	B7 Parameter
NS1	1567
NS2	1567
NS3	1567
NS4	1567
NS5	2169
NS6	1553
NS7	1553
NS8	1553
NS9	1553
NS10	1553
NS11	1621
NS12	1621
NS13	1621
NS14	1621
NS15	1686
NS16	1686
NS17	46
NS18	46
NS19	2482
NS20	1581
NS21	2186
Mean (μ)	**1542.80**
Standard Deviation (σ)	**558.50**

I. DETERMINING RELATIONSHIPS AMONG NON-SUBSTATION SAMPLES

At this stage, a dataset corresponding to the all-non-substation samples were constituted as indicated in Table 17 and the correlations of these substations are given in Fig. 13.

J. RECOGNITION OF SUBSTATIONS BY EMPLOYING LOGIT-BOOST ALGORITHM

At this stage, firstly, data sets belonging to two different classes obtained from substations and non-substation samples were combined. Training and test sets were then created with the leave-one-out cross validation approach. Finally, automatic recognition of substations was performed using the Logit-Boosting algorithm and different spectral

TABLE 16. Generating a dataset for all substations.

Label	Band 1	Band 2	Band 3	Band 4	Band 5	Band 6	Band 7
S1	544	774	1298	1564	3780	3274	2273
S2	521	746	1222	1453	3413	2884	1927
S3	544	774	1298	1564	3780	3274	2273
S4	511	698	1190	1454	3496	2825	1962
S5	640	908	1456	1817	2943	2995	2362
S6	419	598	1056	1198	3474	2595	1623
S7	511	698	1190	1454	3496	2825	1962
S8	511	698	1190	1454	3496	2825	1962
S9	795	1068	1652	2078	3183	3206	2605
S10	576	845	1405	1682	3128	2944	2294
S11	400	574	1032	1106	3654	2445	1655
S12	640	908	1456	1817	2943	2995	2362
S13	643	897	1450	1832	3292	3185	2319
S14	795	1068	1652	2078	3183	3206	2605
S15	795	1068	1652	2078	3183	3206	2605
S16	618	861	1329	1798	3245	3435	2319
S17	652	879	1359	1740	3758	3421	2206
S18	666	889	1378	1844	3904	3407	2163
S19	586	736	1232	1427	3284	3029	2208
S20	394	534	952	977	3619	2532	1541
S21	349	409	711	601	3834	2024	1057
S22	533	709	1131	1380	3497	2915	1949
S23	704	931	1420	1889	3231	3230	2356
S24	378	575	1047	1162	3556	2484	1660
S25	613	812	1231	1702	3239	3157	2024
S26	471	653	1058	1369	3794	3072	1763
S27	613	812	1231	1702	3239	3157	2024
S28	525	694	1076	1363	3213	2947	1939
S29	655	822	1268	1593	3042	3342	2482
S30	471	580	959	1043	3017	2229	1557
S31	585	686	1023	1262	2151	2503	2025
S32	570	756	1245	1475	2874	3028	2183
S33	471	636	1023	1272	3449	2989	1877
S34	585	821	1326	1669	3627	3063	2022
S35	568	703	1101	1347	2847	2454	1844
S36	568	703	1101	1347	2847	2454	1844
S37	410	530	894	1044	3322	2652	1703
S38	404	492	825	954	3087	2550	1667
S39	324	429	696	791	2673	1881	1154
S40	481	630	998	1111	2767	2213	1609
S41	384	487	849	907	3890	2484	1378
S42	388	531	950	1046	3239	2285	1474

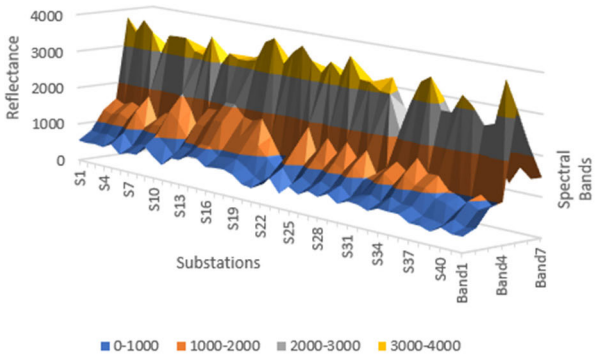

FIGURE 12. The relationship among substations versus the spectral bands with reflectance values.

TABLE 17. Creating a dataset for all non-substation objects.

Label	Band 1	Band 2	Band 3	Band 4	Band 5	Band 6	Band 7
NS1	462	627	943	1248	3265	2685	1567
NS2	462	627	943	1248	3262	2685	1567
NS3	462	627	943	1248	3265	2685	1567
NS4	462	627	943	1248	3265	2685	1567
NS5	661	877	1337	1853	3745	3522	2169
NS6	433	586	965	1143	2922	2395	1553
NS7	433	586	965	1143	2922	2395	1553
NS8	433	586	965	1143	2922	2395	1553
NS9	433	586	965	1143	2922	2395	1553
NS10	433	586	965	1143	2922	2395	1553
NS11	392	509	793	912	2838	2481	1621
NS12	392	509	793	912	2838	2484	1621
NS13	392	509	793	912	2838	2481	1621
NS14	392	509	793	912	2838	2481	1621
NS15	455	618	982	1189	3392	2744	1686
NS16	455	618	982	1189	3392	2744	1686
NS17	493	545	666	266	118	64	46
NS18	493	545	666	266	118	64	46
NS19	726	902	1300	1717	2869	3331	2482
NS20	472	660	1069	1409	3354	2723	1581
NS21	630	867	1354	1727	2948	2928	2186

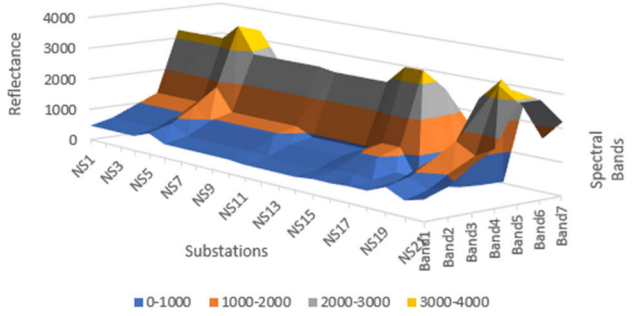

FIGURE 13. The relationship among non-substation samples versus the spectral bands with reflectance values.

TABLE 18. Performance metrics for substation recognition by employing Logit-Boost algorithm and different spectral band parameters.

Feature Sets	Sensitivity (%)	Specificity (%)	Precision (%)	F1-Score (%)	Accuracy (%)
B1	80.95	88.09	77.27	79.06	85.71
B2	80.95	85.71	73.91	77.27	84.12
B3	80.95	90.47	80.95	80.95	87.30
B4	90.47	83.33	73.07	80.85	85.71
B5	80.95	90.47	80.95	80.95	87.30
B6	80.95	92.85	85	82.92	**88.89**
B7	85.71	80.95	69.23	76.59	82.54

band parameters. The performance metrics of the proposed system are shown in Table 18.

K. RECOGNITION OF SUBSTATIONS BY EMPLOYING LSTM

In this section, Table 15 and Table 16 were combined to create a data set. A 'Class' column was created in the data set, containing the value 1 for the values in Table 15 and 0 for the values in Table 16. The success of the system was measured by applying the LSTM model to this data set. Three

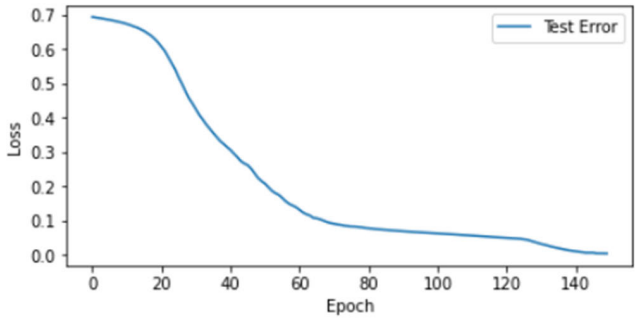

FIGURE 14. The test error graph for LSTM method.

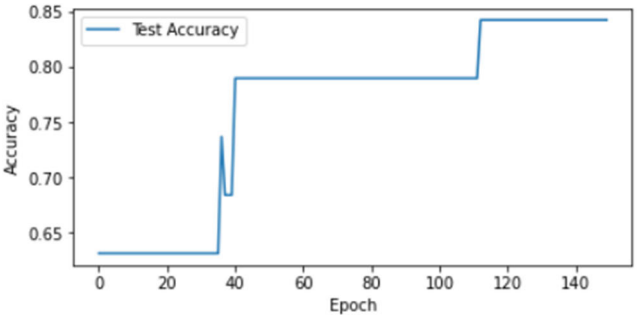

FIGURE 15. The test accuracy graph for LSTM method.

figures containing the ROC curve, Accuracy and Loss Graph, Confusion Matrix and Accuracy rate of the model are given in Fig. 14, Fig. 15, Fig. 16 and Fig. 17, respectively.

As shown in Fig. 14, the error level of the system for the LSTM model decreases with the number of epochs. However, the error rate is stable at approximately 140-150 cycles. For this reason, the number of epochs was chosen as 150.

As seen in Fig. 15, the accuracy level of the system for the LSTM model increases with the number of epochs. As in Fig. 14, it can be observed from this figure that the optimum value for the number of epochs is around 140-150.

The ROC curve shown in Fig. 16 includes TPR and FPR values. When the ROC curve is analyzed, it is observed that the system is at an acceptable level.

When Fig. 17 is observed, the model successfully predicted 16 out of 19 values of the test data correctly. Additionally, as can be seen from the confusion matrix, the number of samples for testing is 19. The total number of samples in the data set is 63. This shows that 70% of the data is used for training and 30% for testing. The success rate of the LSTM method is 84.21%.

IV. DISCUSSION

At this stage, statistical analysis of different spectral band parameters corresponding to substation and non-substation samples was discussed and the effects of these band parameters on automatic substation recognition were examined separately.

TABLE 19. Performance metrics for substation recognition by employing Logit-Boost algorithm and different spectral band parameters.

Reference	Object	Sensor	Technique	Accuracy (%)
Boonpook et al. (2023) [30]	Land	Landsat-8	Deep Learning Semantic Segmentation Algorithm	83-89
Sari et al. (2023) [31]	Urban Environment	Landsat-8	ANN	89
Gharbia (2023) [32]	Water Body Extraction	Landsat-8	RCNN- CNN	80-98
Praticò et al. (2021) [33]	Forest Habitats	Sentinel-2	RF+SVM	80-88
Acar et al. (2021)	Agricultural Crops	Landsat-8	NDVI+SVM	83.30
Balogun et al. (2020)	Oil Spills	Landsat-8	SVM+RF	93.81
Sekandari et al. (2020)	Zn-Pb Mineralization	Sentinel-2, ASTER, Landsat-8 and WorldView-3	PCA+ Fuzzy Logic	70-86.60
Beiranvand Pour et al. (2019)	Mineral	ASTER, Landsat-8 and WorldView-3	DPCA+LSU+ACE	65-77
Golhani et al. (2019)	Oil Palm	Hyperspectral Spectroradiometer	MLPNN	-
Proposed Approach	**Substations**	**Landsat-8**	**B6+Logit Boosting +LSTM**	**84.21-88.89**

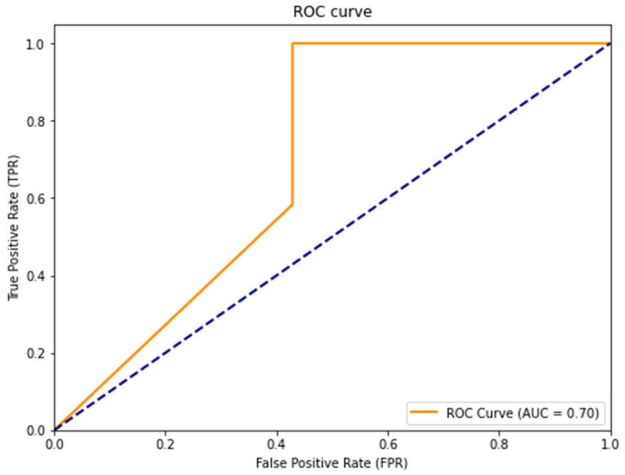

FIGURE 16. The Roc curve for LSTM method.

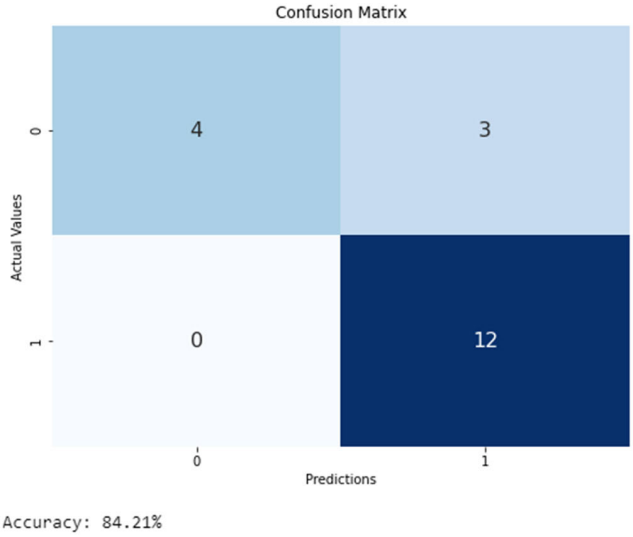

FIGURE 17. The confusion matrix and accuracy rate for LSTM method.

When all the tables between Table 2 and Table 15 are considered, it is seen that the mean and standard deviation of the spectral values in each band of all substations are close to each other. This situation is similar for all non-substation samples between Table 2 and Table 15. The reason for this can be explained as similar objects show similar reflection. However, when the mean and standard deviations of the spectral values in each band belonging to substations and non-substations are compared with each other, it can be said that objects belonging to these two classes differ from each other depending on their reflectance values as illustrated in Fig.12 and Fig.13.

Considering the performance metrics in Table 18, it was observed that the highest average accuracy value was computed as 88.9% by utilizing B6 band parameters and Logit-Boosting algorithm. The confusion matrix for this scenario is given in Fig.14. The reason for this may be that the reflection values of different objects can be distinguished more sharply at the Shortwave Infrared 1 wavelength. Because, this wavelength is usually used for discriminating moisture content of soil and vegetation.

As seen in Fig.14, Fig.15, Fig.16 and Fig.17, high success rates were obtained by using the LSTM method in the proposed approach. Due to the low number of data, deep learning systems can sometimes give low success levels. In such cases, the model layers should be well tuned and overlearning should be avoided. The situation is different in data sets with high amount of data. Overlearning rarely occurs. High accuracy values can be achieved with fewer cycles. Although the data in the data set obtained with the existing substations in the studied area is limited, very successful results have been obtained.

Considering the studies in the literature, there is no similar study on recognizing substations with the help of passive satellite image, machine learning approaches and LSTM method. For this reason, while creating the comparison table below, studies on the detection of different objects using machine learning techniques, LSTM method and passive satellite systems are included as seen in Table 19.

V. CONCLUSION

The use of geographical information systems together with remote sensing techniques is extremely important in the determination of spectral band parameters of various objects. In this study, different spectral band parameters of the Landsat-8 OLI images have been determined in order to determine relationships among the 42 substations and 21 non-substation objects.

The proposed work consists of several stages. In the first stage, the terrains on the Sason district of Batman province were chosen as the study area. In the second stage, the positions of the 42 substations and 21 non-substation objects have been registered thanks to GPS equipment and the GPS data have been then imported to the Landsat-8 OLI images In the next stage, image analysis was performed to calculate spectral band parameters from Landsat-8 OLI data. In addition, utilizing the statistical metrics of the obtained spectral band parameters, the relations among the substations and non-substation objects were established.

Therefore, the feature extraction step, which is essential for the automatic identification of substations, has been accomplished to form datasets. In the last stage, automatic recognition of substations has been performed with high average accuracy by employing obtained dataset, Logit-Boosting algorithm and LSTM method.

When compared with similar studies in the literature, this study achieved high success rates and addresses a previously unexplored subject. The models employed are some of the most popular recently, and it was observed that the detection of substations using Landsat-8 satellite can be done with great accuracy through the LSTM model and Logit-Boost algorithm. Of course, it is worth pointing out that these success rates may increase further by using larger datasets.

As a continuation of this work in the future, it is planned to detect the substations by different spectral band parameters obtained from various satellite data with the aid of different deep learning and machine learning methods With this proposed study, it is thought to prevent illegal electricity consumption.

DECLARATIONS CONFLICTS OF INTEREST

The authors declared that there is no conflict of interest regarding this work.

ACKNOWLEDGMENT

The authors wish to thank Dicle Electricity Distribution Company.

REFERENCES

[1] G. Cheng and J. Han, "A survey on object detection in optical remote sensing images," *ISPRS J. Photogramm. Remote Sens.*, vol. 117, pp. 11–28, Jul. 2016.

[2] B. B. Bilgilioğlu, R. Çömert, O. Yigit, and F. Bedir, "Yüksek mekânsal çözünürlüklü uydu görüntülerinden nesne tabanlý sýnýflandýrma yaklasimi ile çay bahçelerinin çýkarýlmasý," *Turk J. Remote Sens.*, vol. 1, no. 1, pp. 21–27, 2019.

[3] H. Acar, M. S. Ozerdem, and E. Acar, "Soil moisture inversion via semiempirical and machine learning methods with full-polarization Radarsat-2 and polarimetric target decomposition data: A comparative study," *IEEE Access*, vol. 8, pp. 197896–197907, 2020.

[4] E. Acar and M. Altun, "Classification of the agricultural crops using Landsat-8 NDVI parameters by support vector machine," *Balkan J. Electr. Comput. Eng.*, vol. 9, no. 1, pp. 78–82, Jan. 2021.

[5] A.-L. Balogun, S. T. Yekeen, B. Pradhan, and O. F. Althuwaynee, "Spatio-temporal analysis of oil spill impact and recovery pattern of coastal vegetation and wetland using multispectral satellite Landsat 8-OLI imagery and machine learning models," *Remote Sens.*, vol. 12, no. 7, p. 1225, Apr. 2020.

[6] M. Sekandari, I. Masoumi, A. B. Pour, A. M. Muslim, O. Rahmani, M. Hashim, B. Zoheir, B. Pradhan, A. Misra, and S. M. Aminpour, "Application of Landsat-8, Sentinel-2, ASTER and WorldView-3 spectral imagery for exploration of carbonate-hosted pb-zn deposits in the central Iranian terrane (CIT)," *Remote Sens.*, vol. 12, no. 8, p. 1239, Apr. 2020.

[7] Q. Vanhellemont, "Automated water surface temperature retrieval from Landsat 8/TIRS," *Remote Sens. Environ.*, vol. 237, Feb. 2020, Art. no. 111518.

[8] A. B. Pour, T. Y. Park, Y. Park, J. K. Hong, A. M. Muslim, A. Laufer, L. Crispini, B. Pradhan, B. Zoheir, O. Rahmani, and M. Hashim, "Landsat-8, advanced spaceborne thermal emission and reflection radiometer, and WorldView-3 multispectral satellite imagery for prospecting copper-gold mineralization in the northeastern inglefield mobile belt (IMB), Northwest Greenland," *Remote Sens.*, vol. 11, no. 20, p. 2430, Oct. 2019.

[9] K. Golhani, S. K. Balasundram, G. Vadamalai, and B. Pradhan, "Selection of a spectral index for detection of orange spotting disease in oil palm (*Elaeis guineensis Jacq.*) using red edge and neural network techniques," *J. Indian Soc. Remote Sens.*, vol. 47, no. 4, pp. 639–646, Apr. 2019.

[10] X. Fan, G. Nie, Y. Deng, J. An, J. Zhou, C. Xia, and X. Pang, "Estimating earthquake-damage areas using Landsat-8 OLI surface reflectance data," *Int. J. Disaster Risk Reduction*, vol. 33, pp. 275–283, Feb. 2019.

[11] B.-J. He, Z.-Q. Zhao, L.-D. Shen, H.-B. Wang, and L.-G. Li, "An approach to examining performances of cool/hot sources in mitigating/enhancing Land Surface Temperature under different temperature backgrounds based on Landsat 8 image," *Sustain. Cities Soc.*, vol. 44, pp. 416–427, Jan. 2019.

[12] W. Fang, C. Wang, X. Chen, W. Wan, H. Li, S. Zhu, Y. Fang, B. Liu, and Y. Hong, "Recognizing global reservoirs from Landsat 8 images: A deep learning approach," *IEEE J. Sel. Topics Appl. Earth Observ. Remote Sens.*, vol. 12, no. 9, pp. 3168–3177, Sep. 2019.

[13] C. Kuhn, A. de Matos Valerio, N. Ward, L. Loken, H. O. Sawakuchi, M. Kampel, J. Richey, P. Stadler, J. Crawford, R. Striegl, E. Vermote, N. Pahlevan, and D. Butman, "Performance of Landsat-8 and Sentinel-2 surface reflectance products for river remote sensing retrievals of chlorophyll-a and turbidity," *Remote Sens. Environ.*, vol. 224, pp. 104–118, Apr. 2019.

[14] A. Lamqadem, H. Saber, and B. Pradhan, "Quantitative assessment of desertification in an arid oasis using remote sensing data and spectral index techniques," *Remote Sens.*, vol. 10, no. 12, p. 1862, Nov. 2018.

[15] M. I. Sameen, B. Pradhan, and O. S. Aziz, "Classification of very high resolution aerial photos using spectral–spatial convolutional neural networks," *J. Sensors*, vol. 2018, pp. 1–12, Jun. 2018, doi: 10.1155/2018/7195432.

[16] C. D. Man, T. T. Nguyen, H. Q. Bui, K. Lasko, and T. N. T. Nguyen, "Improvement of land-cover classification over frequently cloud-covered areas using Landsat 8 time-series composites and an ensemble of supervised classifiers," *Int. J. Remote Sens.*, vol. 39, no. 4, pp. 1243–1255, Feb. 2018.

[17] N. Arslan, "Assessment of oil spills using sentinel 1 C-band SAR and Landsat 8 multispectral sensors," *Environ. Monitor. Assessment*, vol. 190, no. 11, p. 637, Nov. 2018.

[18] H. Wang, Z. Zou, Z. Shi, and B. Li, "Detecting ship targets in spaceborne infrared image based on modeling radiation anomalies," *Infr. Phys. Technol.*, vol. 85, pp. 141–146, Sep. 2017.

[19] B. B. Barnes and C. Hu, "Island building in the South China sea: Detection of turbidity plumes and artificial islands using Landsat and MODIS data," *Sci. Rep.*, vol. 6, no. 1, p. 33194, Sep. 2016.

[20] U. Avdan and G. Jovanovska, "Algorithm for automated mapping of Land Surface Temperature using Landsat 8 satellite data," *J. Sensors*, vol. 2016, pp. 1–8, Jan. 2016, doi: 10.1155/2016/1480307.

[21] M. Wieland and M. Pittore, "Large-area settlement pattern recognition from Landsat-8 data," *ISPRS J. Photogramm. Remote Sens.*, vol. 119, pp. 294–308, Sep. 2016.

[22] P. Jagalingam, B. J. Akshaya, and A. V. Hegde, "Bathymetry mapping using Landsat 8 satellite imagery," *Proc. Eng.*, vol. 116, pp. 560–566, Jan. 2015.

[23] E. Acar, "Detection of unregistered electric distribution transformers in agricultural fields with the aid of Sentinel-1 SAR images by machine learning approaches," *Comput. Electron. Agricult.*, vol. 175, Aug. 2020, Art. no. 105559.
[24] N. Gorelick, M. Hancher, M. Dixon, S. Ilyushchenko, D. Thau, and R. Moore, "Google Earth engine: Planetary-scale geospatial analysis for everyone," *Remote Sens. Environ.*, vol. 202, pp. 18–27, Dec. 2017.
[25] M. Montanaro, A. Gerace, A. Lunsford, and D. Reuter, "Stray light artifacts in imagery from the Landsat 8 thermal infrared sensor," *Remote Sens.*, vol. 6, no. 11, pp. 10435–10456, Oct. 2014.
[26] J. Friedman, T. Hastie, and R. Tibshirani, "Additive logistic regression: A statistical view of boosting (with discussion and a rejoinder by the authors)," *Ann. Statist.*, vol. 28, no. 2, pp. 337–407, Apr. 2000.
[27] Y. Yang, Q. Fu, and D. Wan, "A prediction model for time series based on deep recurrent," *Comput. Technol. Dev.*, vol. 27, no. 3, pp. 35–38, 2017.
[28] Y. Chen, S. Zhang, W. Zhang, J. Peng, and Y. Cai, "Multifactor spatio-temporal correlation model based on a combination of convolutional neural network and long short-term memory neural network for wind speed forecasting," *Energy Convers. Manag.*, vol. 185, pp. 783–799, Apr. 2019.
[29] W. Zha, Y. Liu, Y. Wan, R. Luo, D. Li, S. Yang, and Y. Xu, "Forecasting monthly gas field production based on the CNN-LSTM model," *Energy*, vol. 260, Dec. 2022, Art. no. 124889.
[30] W. Boonpook, Y. Tan, A. Nardkulpat, K. Torsri, P. Torteeka, P. Kamsing, U. Sawangwit, J. Pena, and M. Jainaen, "Deep learning semantic segmentation for land use and land cover types using Landsat 8 imagery," *ISPRS Int. J. Geo-Information*, vol. 12, no. 1, p. 14, Jan. 2023.
[31] N. M. Sari, D. Kushardono, M. Mukhoriyah, K. Kustiyo, and M. D. M. Manessa, "Optimized artificial neural network for the classification of urban environment comfort using Landsat-8 remote sensing data in greater Jakarta area, Indonesia," *J. Appl. Eng. Technol. Sci. (JAETS)*, vol. 4, no. 2, pp. 743–755, Jun. 2023.
[32] R. Gharbia, "Deep learning for automatic extraction of water bodies using satellite imagery," *J. Indian Soc. Remote Sens.*, vol. 51, no. 7, pp. 1511–1521, Jul. 2023.
[33] S. Praticò, F. Solano, S. Di Fazio, and G. Modica, "Machine learning classification of Mediterranean forest habitats in Google Earth engine based on seasonal Sentinel-2 time-series and input image composition optimisation," *Remote Sens.*, vol. 13, no. 4, p. 586, Feb. 2021.

EMRULLAH ACAR received the B.S. degree in electrical and electronics engineering from Çukurova University, Adana, Turkey, in 2009, the first M.S. degree in biomedical engineering from Istanbul Technical University, Istanbul, Turkey, in 2010, and the second M.S. and Ph.D. degrees in electrical and electronics engineering from Dicle University, Diyarbakır, Turkey, in 2012 and 2017, respectively. He is currently an Associate Professor of electrical and electronics engineering with Batman University and also the Head of the Electronics Division. He received awards and honors, include the Scientific and Technological Research Council of Turkey (TUBITAK) Grant; Erasmus Mobility Grant, Sweden; and Erasmus Internship Grant, Germany. His research interests include digital image processing, machine learning, and remote sensing applications.

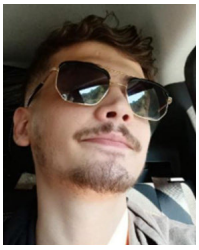

ENES BAKIŞ received the B.S. degree in electrical and electronics engineering from Batman University, Batman, Turkey, in 2021, and the M.S. degree in electrical and electronics engineering from Batman University, where he is currently pursuing the Ph.D. degree in electrical and electronics engineering. He currently works as a Research Assistant at Piri Reis University, Istanbul. His research interests include digital image processing, machine learning, deep learning, and remote sensing applications.

MUSA YILMAZ (Senior Member, IEEE) received the M.Sc. and Ph.D. degrees in electrical education from Marmara University, Istanbul, Turkey, in 2004 and 2013, respectively. He currently holds the position of an Assistant Professor with the Electrical and Electronics Engineering Department and the Energy Engineering Department, Batman University. From 2015 to 2016, he joined the Smart Grid Research Center (SMERC), The University of California, Los Angeles (UCLA), as a Visiting Scholar. He has conducted extensive research in the field of smart grids and solar energy. Along with Biosys LLC, he is an inventor of a ventilator class named "Biyovent." He has made significant contributions to academia and publishing. Additionally, he is a Co-Founder of INESEG, a publishing organization. He has authored over 50 research articles, several book chapters, and frequently delivers invited keynote lectures at international conferences. He has also led his research team as the principal investigator in several European projects. His primary research interests revolve around smart grid technologies and renewable energy. He served as the Editor-in-Chief for the *Balkan Journal of Electrical and Computer Engineering* (BAJECE) and the *European Journal of Technique* (EJT).